Editors' Suggestion

Guiding diamond spin qubit growth with computational methods

Jonathan C. Marcks,[1,2,*] Mykyta Onizhuk,[3,1,*] Nazar Delegan,[2,1] Yu-Xin Wang (王语馨),[1] Masaya Fukami,[1] Maya Watts,[2,1] Aashish A. Clerk,[1] F. Joseph Heremans,[2,1] Giulia Galli,[1,3,2] and David D. Awschalom[1,4,2,†]

[1]*Pritzker School of Molecular Engineering, University of Chicago, Chicago, Illinois 60637, USA*

[2]*Center for Molecular Engineering and Materials Science Division, Argonne National Laboratory, Lemont, Illinois 60439, USA*

[3]*Department of Chemistry, University of Chicago, Chicago, Illinois 60637, USA*

[4]*Department of Physics, University of Chicago, Chicago, Illinois 60637, USA*

(Received 13 August 2023; accepted 31 January 2024; published 28 February 2024)

The nitrogen-vacancy (NV) center in diamond, a well-studied, optically active spin defect, is the prototypical system in many state-of-the-art quantum sensing and communication applications. In addition to the enticing properties intrinsic to the NV center, its diamond host's nuclear and electronic spin baths can be leveraged as resources for quantum information rather than considered solely as sources of decoherence. However, current synthesis approaches result in stochastic defect spin positions, reducing the technology's potential for deterministic control and yield of NV spin bath systems, as well as scalability and integration with other technologies. Here, we demonstrate the use of theoretical calculations of electronic central spin decoherence as an integral part of an NV spin bath synthesis workflow, providing a path forward for the quantitative design of NV center-based quantum sensing systems. We use computationally generated coherence data to characterize the properties of single NV center qubits across relevant growth parameters to find general trends in coherence time distributions dependent on spin bath dimensionality and density. We then build a maximum likelihood estimator with our theoretical model, enabling the characterization of a test sample through NV T_2^* measurements. Finally, we explore the impact of dimensionality on the yield of strongly coupled electron spin systems. The methods presented herein are general and applicable to other qubit platforms that can be appropriately simulated.

DOI: 10.1103/PhysRevMaterials.8.026204

I. INTRODUCTION

Defect color centers in diamond [1,2] have been demonstrated as quantum magnetometers [3–11] and nodes in quantum communication networks [12–16]. Quantum applications of the negatively charged nitrogen-vacancy (NV) center, with a spin-photon interface and coherent operation up to and above room temperature [1,17–19], will benefit from interfacing the central NV spin qubit with accessible dark spins in the diamond lattice for quantum memories [20–22] and many-body metrological states [23–25]. These applications could enable scalable quantum networks and quantum sensing beyond the standard quantum limit. Explorations of such multispin systems have relied on NV centers that are either naturally occurring [15,16,21,22,26,27], precluding scalability, or that are formed via nitrogen implantation [28–35], introducing qubit decoherence sources, associated with crystal damage [36].

Diamond-based quantum applications benefit greatly from the ongoing optimization of bottom-up color center synthesis via plasma-enhanced chemical vapor deposition (PECVD) [37–40]. Delta (δ) doping studies [41–43] have demonstrated vacancy diffusion-limited spatially localized NV centers, while avoiding the crystal damage and processing inherent to aperture mask or focused implantation [42,44–49]. PECVD of diamond quantum systems has enabled engineering of NV center spin environments via isotopic purification [41,50,51], dimensionality control [41,52,53], and codoping techniques [54–56]. However, the development of these techniques has outpaced computational efforts to model spin-bath-induced decoherence [57,58], and theoretical approaches have not yet been applied to investigate diamond qubit synthesis. Cluster correlation expansion (CCE) methods provide an accurate approach to model decoherence in varied and tailored electron and nuclear spin bath environments [59]. Such methods have recently been applied to study material systems relevant for quantum applications [58,60–62], indicating that CCE may indeed be a powerful tool to enable more efficient synthesis procedures, which are crucial for the design of quantum materials [63].

In this work, we apply CCE methods, as implemented in the open source framework PyCCE [60], to predict and characterize bottom-up solid-state spin qubit synthesis. We first introduce the computation and materials growth techniques. We then explore a common electronic spin defect created during NV center synthesis: the neutrally charged substitutional nitrogen N_s^0 with electron spin $S = \frac{1}{2}$ (P1 center). Using theoretical predictions, we investigate the P1 center electron spin-bath-induced decoherence [57,64] of NV centers in diamond across the parameter space of our growth regime (P1 density and layer thickness). We focus on low-dimensional spin bath geometries, finding central spin lifetime-limited coherence times and a nontrivial dependence of single-spin coherence times on dimensionality. Obtained dependencies enable the

*These authors contributed equally to this work.
†Corresponding author: awsch@uchicago.edu

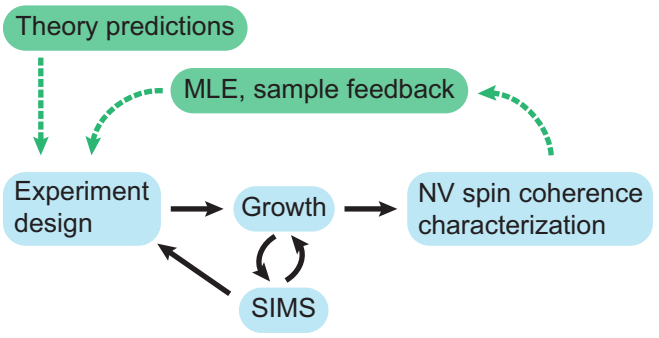

FIG. 1. Growth process workflow. The current process steps (blue) for synthesizing a diamond NV sample. Iterations of growth and SIMS analysis are required to confirm nitrogen doping densities. The theoretical predictions and density maximum likelihood estimation (MLE) model in this work (green) enable a nondestructive feedback process to circumvent SIMS and allow for an efficient experimental design.

use of coherence time distributions as descriptors of these systems for determining the growth parameters. To this end, we develop a maximum likelihood estimation (MLE) model based on Ramsey T_2^* coherence times and apply it to characterize nitrogen incorporation in an experimental test sample. We then study low-dimensional electron spin baths as hosts to strongly coupled electron spin systems, demonstrating how our computational techniques can help improve the yield of future quantum devices and aid in experimental design.

In Fig. 1, we show the strategy adopted in this work to improve upon the current NV synthesis and experiment design process. The blue boxes show the commonly adopted process for generating single NV centers. After identifying a desired sample density and geometry, iterations of growth and secondary ion mass spectrometry (SIMS) are necessary to confirm the nitrogen doping density. In practice, we have observed large variations in SIMS results that reduce the efficacy of this approach, as discussed in Sec. II B. Here, we show that it is beneficial to incorporate theoretical spin bath predictions as well as an *in situ* density characterization tool into our workflow (green boxes). The understanding of low-dimensional spin bath decoherence obtained through theory and computation improves initial experiment design, and the local density feedback enabled by the MLE model circumvents the need for SIMS characterizations of doping density. This method for *in situ* measurement of spin bath density additionally opens a path to study postgrowth modification of spin bath environments [65].

II. RESULTS

A. Validation of theoretical calculations

Within the CCE approach [66,67] the coherence function $\mathcal{L}(t) = \frac{\langle 0|\hat{\rho}(t)|1\rangle}{\langle 0|\hat{\rho}(0)|1\rangle}$, defined as the normalized off-diagonal element of the density matrix of the qubit $\hat{\rho}(t)$, is approximated as a product of irreducible contributions of bath spin clusters, where the maximum size of the cluster n corresponds to the order n of the CCEn approximation [Fig. 2(a)]. We converge

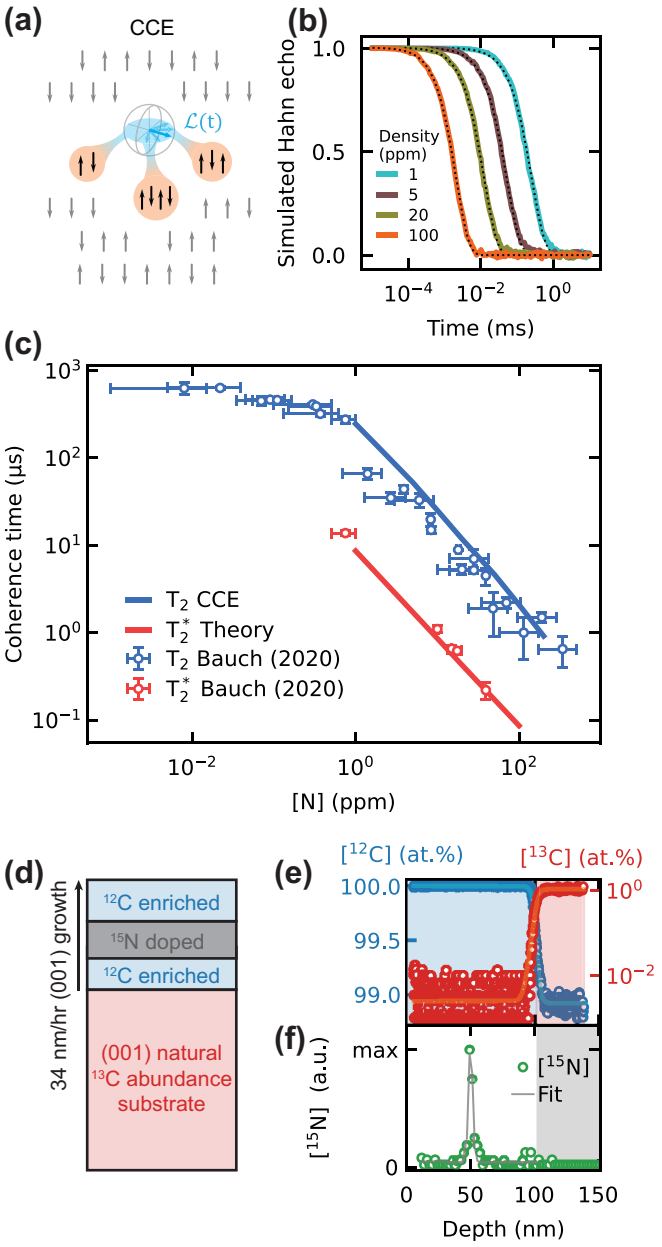

FIG. 2. Computational and diamond growth methods. (a) Schematic representation of the cluster correlation expansion (CCE) approach. (b) Example of the Hahn-echo coherence calculated using the PyCCE code [60] for various ^{14}N P1 spin baths. The values of T_2 times are extracted from a stretched exponential fit of the form $\exp[-(\frac{t}{T_2})^n]$ (dashed line). (c) T_2 and T_2^* coherence times overlaid with corresponding experimental data [57], validating our computational methods. (d) Schematic of isotopically pure (^{12}C) PE-CVD (100) diamond overgrowth with isotopically tagged ^{15}N nitrogen δ doping. This sample geometry with varying nitrogen incorporation density and thickness is considered throughout this paper. (e), (f) Carbon (top) and nitrogen (bottom) isotope concentrations measured via SIMS on characterization sample, demonstrating isotopic purification of host material and isotopically tagged nitrogen incorporation. Carbon SIMS is used to calibrate the growth rate, shown in (d). The nitrogen concentration is quantified with NV coherence measurements in Sec. II E.

the calculations with respect to the size of the bath and the order of CCE approximation. We find that the Ramsey signal of the electron spin in the electron spin bath is converged at first order (CCE1), when each P1 is treated as an isolated spin. We can thus solve the P1-limited Ramsey decoherence analytically and compute T_2^* as a sum of the couplings between the NV center and the weakly coupled P1 centers. The Hahn-echo signal is instead simulated at the CCE4 level of theory (see Methods for more details).

We validate our theoretical calculations against a reference data set of NV center ensemble coherence times in bulk ^{14}N P1 spin baths [57]. We extract T_2 from the coherence curve by fitting the signal to a stretched exponential function $\exp[-(\frac{t}{T_2})^n]$, as shown in Fig. 2(b). Computed ensemble T_2^* and T_2, averaged over a set of random P1 positions, are overlaid in Fig. 2(c) with experimental data, taken from Ref. [57]. We find excellent agreement with the experimental data in the P1-limited coherence regime, showing that the first-principles calculation with the CCE method yields a quantitative description of the decoherence due to P1 spin baths. The stretched exponent parameter of the computed Hahn-echo decay is between $n = 1.2$–1.3, in excellent agreement with the data of Ref. [57].

B. Diamond growth and defect synthesis

The sample studied in this paper, shown schematically in Fig. 2(d), was grown with a 3-min, 10-sccm $^{15}N_2$ flow at a time corresponding to a depth of ≈50 nm. Nitrogen δ doping is achieved by introducing $^{15}N_2$ gas (99.99 % chemical purity, 99.9 at. % isotopic purity) during diamond growth. According to the SIMS characterization of a calibration sample, shown in Figs. 2(e) and 2(f), this creates a 3.8(2)-nm-thick (compared to $1.3^{+2.2}_{-0}$ nm predicted from growth calibrations) ^{15}N-doped layer at a depth of 50.2(1) nm, with a SIMS-quantified [^{15}N] density of 0.39(2) ppm to 4.16(7) ppm (dependent on third-party SIMS measurement, detailed in the Supplemental Material, Sec. S.II.A [68]) within ^{12}C isotopically purified diamond overgrowth ([^{12}C] = 99.993 at. %). These values are obtained from a calibration sample processed and grown identically to the sample studied in this paper.

While SIMS is often used for detecting low concentrations of dopants in semiconducting materials, sample geometries unique to our application remain difficult to characterize accurately due to experimental limitations. Specifically, the tradeoff between depth resolution and overall sensitivity is dictated by the analysis or sputtering energy. Under our characterization conditions, the ideal detection limits for ^{15}N and ^{14}N densities are 1×10^{15} cm^{-3} (≈0.006 ppm) and 7×10^{15} cm^{-3} (≈0.028 ppm), respectively. However, the obtained densities can vary significantly as a function of sample inhomogeneities, the presence of growth defects, and experimental conditions. While studying samples that were nominally grown under the same conditions, SIMS quantification of [^{15}N] has been observed to regularly vary by at least an order of magnitude, requiring rigorous statistics over growth of multiple samples, a time- and resource-consuming process. A truly local spin-defect materials characterization method is necessary, motivating the *in situ* maximum likelihood estimation of the density characterization presented in Sec. II E, a capability enabled by our computational results. A recently developed complementary approach analyzes the effect of spin bath density and dimensionality on the shape of the exponential coherence decay of ensembles of NV centers [52,53]. Our approach, in contrast, operates in a single NV center regime, relevant for many NV center applications, and relies on converged, experimentally verified calculations rather than an analytical treatment based on ensemble averaging of individual NV center spin dephasing. Both approaches address the need for accurate characterization of quantum platforms.

C. Single-spin coherence in quasi-2D electron bath

We investigate single-spin coherence properties across the density and thickness parameter space available for the PECVD growth recipe adopted in this work and described in the Methods section (Sec. IV B). We compute Ramsey coherence time T_2^* [Fig. 3(a), left] for 10^5 spin bath configurations with spin bath thickness of 0.5 to 12 nm (0.5-nm steps) and density of 0.5 to 12 ppm (0.5-ppm steps) from the coupling between the central NV center electron spin and weakly coupled P1 center electron spins (see Methods). We simulate Hahn-echo measurements [Fig. 3(a), right] with spin bath thicknesses of 1 to 10 nm (1-nm steps) and densities of 1 to 12 ppm (1-ppm steps) (see Supplemental Material, Sec. S.I.B, for justification of CCE order [68]).

We characterize the distributions of the coherence times with the mean $\mu = 10^{\langle \log_{10}(T_2/[1\,\mathrm{ms}])\rangle}$ and the variance $\sigma^2 = \langle \log_{10}^2(T_2/[1\,\mathrm{ms}])\rangle - \langle \log_{10}(T_2/[1\,\mathrm{ms}])\rangle^2$ of the logarithm of the coherence times at each density and thickness (Fig. 3). Using the coherence time logarithm, we can directly compare the coherence distributions at different timescales.

Figures 3(b), 3(c) and 3(d), 3(e) depict μ and σ over the chosen range of parameters for T_2^* and T_2, respectively. In each case, the computed average coherence time decreases with increasing spin density and/or increasing thickness, as expected. In the three-dimensional limit, the average coherence time is independent of bath thickness. The observed decrease in μ as a function of thickness [Figs. 3(b) and 3(d)] suggests the presence of a low-dimensional spin bath regime in the chosen range of parameters.

We analytically derive the distribution of the interaction strength between the central spin and bath spins in low-dimensional baths in Sec. II F. In the case of T_2 we predict times >1 ms in the bottom-left half of the parameter space in Fig. 3(d), beyond what is generally observed in experiment. This suggests that experimental T_2 times in thin, low-density spin baths are limited by noise sources not captured in our model, as suggested previously [57]. However, our calculations predict that, in principle, low-dimensional lightly doped samples can realize T_1 limited coherence times at room temperature.

Bath dimensionality further impacts the relative distribution of coherence times, described by the standard deviation σ. Focusing on the inhomogeneous dephasing time T_2^* [Fig. 3(c), right], σ exhibits unexpected behavior in the region where the thickness equals the average nearest-neighbor distance in three dimensions, $\langle r_{\mathrm{NN}}\rangle$, plotted as a function of density in the left plot. σ plateaus when the thickness is smaller than $\langle r_{\mathrm{NN}}\rangle$ and decreases when thicknesses are larger.

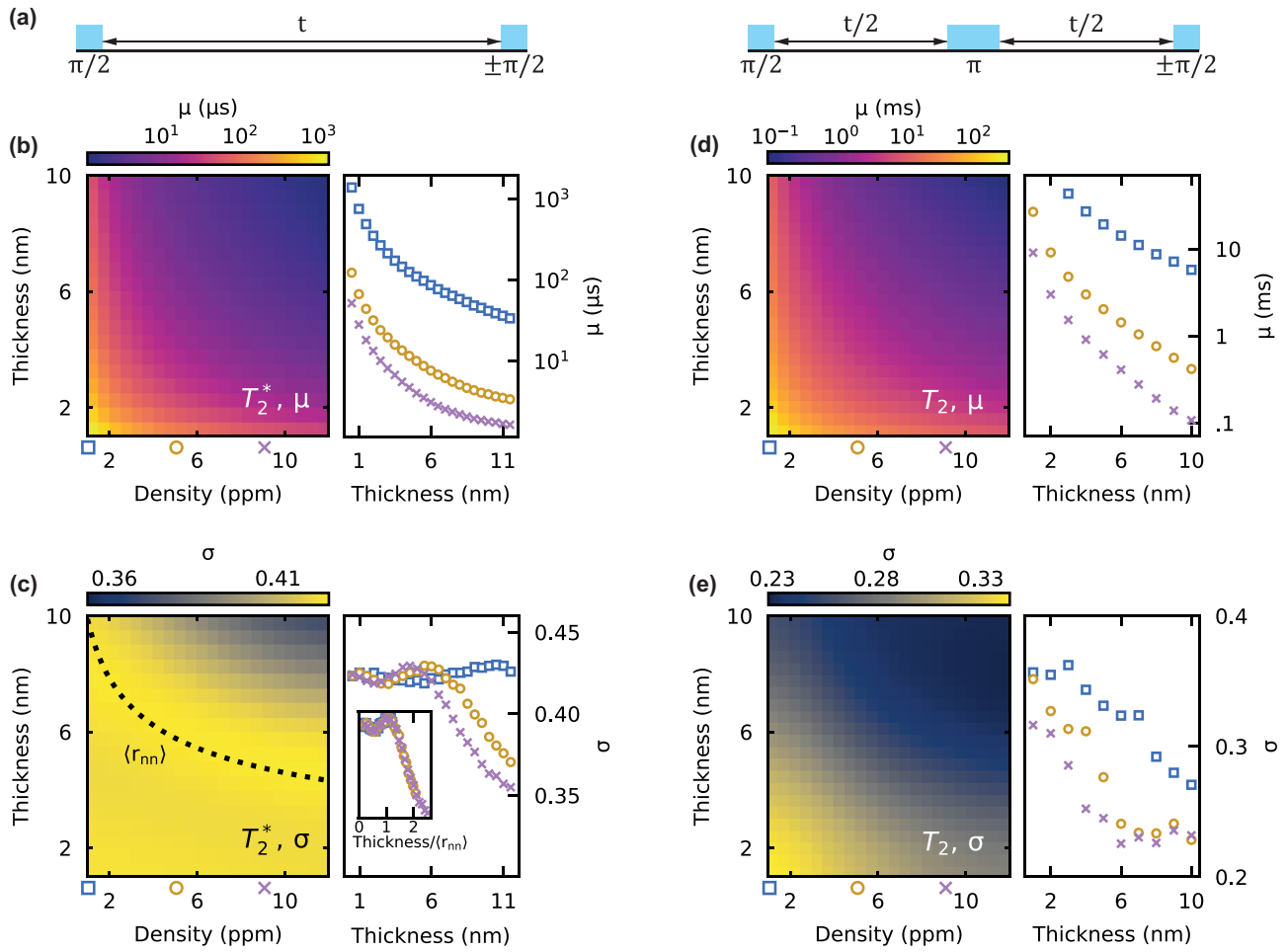

FIG. 3. Single-spin coherence in low-dimensional spin baths. (a) Ramsey (left) and Hahn-echo (right) microwave measurement pulse sequences. (b), (c) Mean of $\log_{10}(T_2^*/[1\,\mathrm{ms}])$ distributions $\mu = 10^{\langle \log_{10}(T_2^*/[1\,\mathrm{ms}])\rangle}$ (b) and variance $\sigma^2 = \langle \log_{10}^2(T_2^*/[1\,\mathrm{ms}])\rangle - \langle \log_{10}(T_2^*/[1\,\mathrm{ms}])\rangle^2$ (c) as a function of P1 density and layer thickness. Values are linearly interpolated between data points. The black dashed line in (c) indicates the thickness equal to the average nearest-neighbor bath spin distance $\langle r_{\mathrm{NN}}\rangle = 0.554\rho^{-1/3}$ for each density ρ (see text, Sec. II F), demonstrating a boundary between dimensionalities. At right in (b) and (c) are line cuts of μ and σ at densities of 1, 5, and 9 ppm. Inset in (c) is σ at multiple densities with thickness normalized by $\langle r_{\mathrm{NN}}\rangle$, demonstrating universal behavior versus dimensionality. (d), (e) The same data as (b) and (c) presented for T_2 coherence times.

The inset in Fig. 3(c), right, demonstrates the universal behavior of coherence times relative to the bath dimensionality. The x axis is normalized to $\langle r_{\mathrm{NN}}\rangle$. This indicates that two-dimensional (2D) spin baths naturally have a wider spread of NV center coherence times. While thin and less dense samples may optimize coherence times, they typically also lead to greater fluctuations in single-qubit coherence properties.

We see similar trends in Hahn-echo T_2 times [Fig. 3(e), right]. We find in general that $\sigma_{T_2^*} > \sigma_{T_2}$. In the Supplemental Material, Sec. S.I.C [68], we find convergence for T_2^* and T_2 at 12 and 100 bath spins, respectively, suggesting heuristically that Ramsey measurements are sensitive to the variation of a fewer number of spins. In general, one expects a smaller standard deviation in physical quantities that are sensitive to larger numbers of randomly placed spins due to the central limit theorem. We thus expect a larger impact of the stochasticity in the P1 position on the T_2^* distributions. These results inform solid-state qubit synthesis characterization, where both T_2^* and T_2 are standard measurements performed on multiple NV centers.

Our theoretical results constitute a full computational characterization of spin-bath-induced coherence times across a range of bath geometries and densities. Our computational strategy is not limited to NV centers in diamond and can be applied to other spin defect systems, as well as other spin bath measurements, as long as the appropriate pulse sequence can be simulated using the PyCCE code. Additionally, our approach will inform future diamond growth and NV synthesis. Rather than extrapolating from bulk data [57] or measurements on single δ-doped NV centers, growth may now be informed by the theoretical predictions of coherence time distributions.

D. Sample characterization

We characterize the coherence of an exemplar sample grown under the conditions outlined in Sec. IV B. Figure 4(a) presents frequency-dependent double electron-electron resonance (DEER) measurements of a single NV center in a P1 center bath. This measurement essentially performs electron spin resonance (ESR) spectroscopy on target spins (here P1

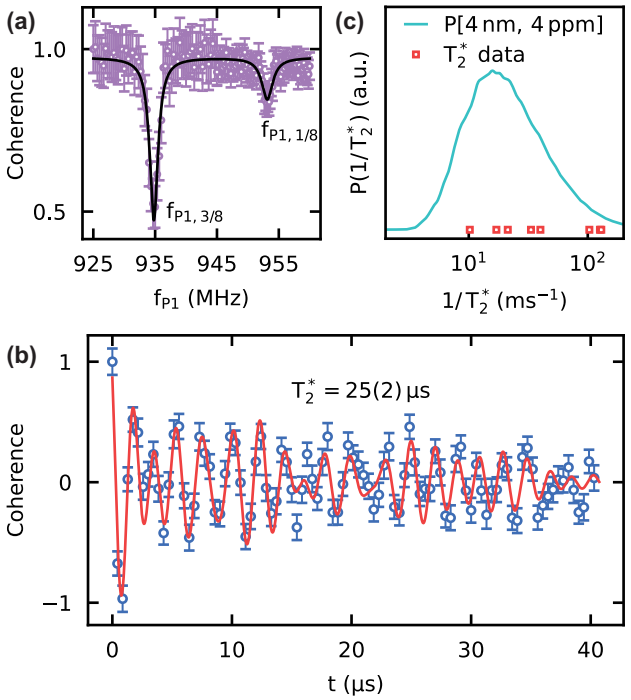

FIG. 4. NV center measurements. (a) DEER spectroscopy with NV center confirming the presence of a P1 center electron spin bath. Marked values of f_{P1} correspond to P1 ESR transitions corresponding to the static magnetic field of 311 G and internal P1 hyperfine parameters. (b) Ramsey interferometry measurement to extract T_2^* coherence time. (c) Compiled decoherence rates for eight measured NV centers (red squares, the two rightmost points overlap) and the probability function P, drawn directly from the histogram of computed coherence times for parameters determined in Sec. II E.

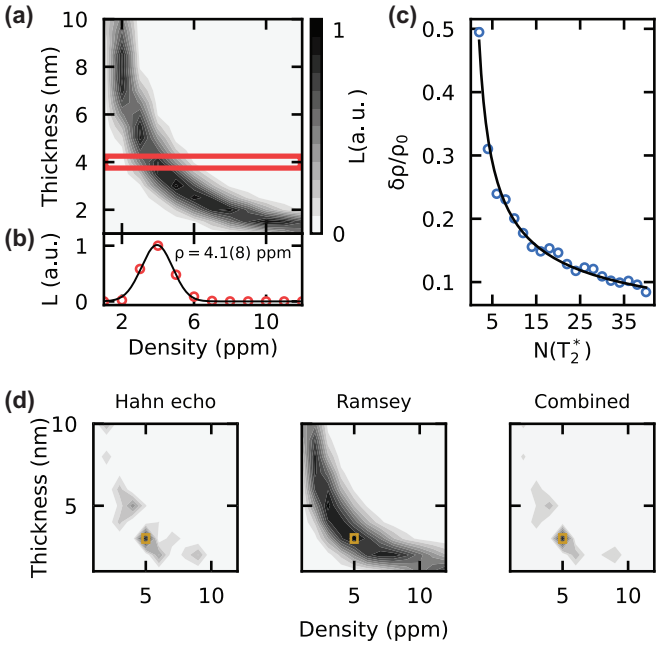

FIG. 5. Maximum likelihood estimation. (a) Likelihood of data set in Fig. 4(c) calculated for each set of bath parameters from theoretical results. (b) Likelihood restricted to a thickness of $t_{SIMS} = 4$ nm [from Fig. 2(e)], from which we extract a density of $4.1 \pm .8$ ppm. (c) Calculated error of density estimation across full density range with fixed thickness, calculated for 200 random data sets at each density. (d) MLEs on a test data set of four NV centers generated from calculations of coherence times for a 3-nm-thick 5-ppm bath. The combined MLE (right), where the likelihood is calculated joint across both data sets, is the most sensitive. Scale bars are the same as in (a).

center electron spins) by recoupling their dipolar interactions to the NV center probe spin, which are otherwise decoupled by the Hahn-echo sequence. At the experimental magnetic field of 311 G, and given ^{15}N P1 hyperfine couplings, we expect, based on the possible P1 Jahn-Teller axis directions and ^{15}N nuclear spin states (see Methods), transitions near 935 MHz and 954 MHz for the four possible ⟨111⟩ crystallographic axes, respectively, and the nitrogen nuclear spin state $+\frac{1}{2}$ probed here. We observe resonances at microwave light frequencies f_{P1} of 934.8 MHz ($f_{P1,3/8}$) and 953.1 MHz ($f_{P1,1/8}$). The subscripts indicate the fraction of the bath probed at that frequency. This confirms the presence of ^{15}N P1 centers in our sample.

We measure T_2^* times for a set of eight single NV centers in the same test sample. Figure 4(b) shows characteristic Ramsey interferometry data for one of these NV centers. Data are fit to a Gaussian decay with oscillations capturing the coupling to single nearby P1 centers, as in the Ramsey analysis in Sec. II. While the ^{15}NV center exhibits a ≈3 MHz splitting from its nitrogen nuclear spin, it does not contribute to NV center decoherence rate and thus is not included in CCE calculations. We are careful to drive with 909 kHz Rabi rate pulses to avoid mixing nuclear hyperfine effects into our measurement. This NV center exhibits $T_2^* = 25 \pm 2$ µs (see Supplemental Material, Sec. S.III, for details of measurements [68]). This process is repeated for eight NV centers.

Decoherence rates for the set of measured NV centers are plotted in Fig. 4(c) along with the calculated probability distribution function (PDF) that best fits the measured distribution as determined via MLE, discussed in the next section. The aim of the following section will be to determine which calculated distribution best fits this data set.

E. Maximum likelihood estimation

Using the theoretical dependence of the coherence time distributions on thickness and P1 density, in this section we develop the maximum likelihood estimation (MLE) model to recover the growth parameters of the given sample. Taking interpolated distributions $P(1/T_2^*)$, recovered from the numerical data, the likelihood of a given bath configuration is calculated as the joint probability of the $\{T_2^*\}$ data set for each pair of bath thickness t and density ρ as [69]

$$L(t, \rho) = \prod_i P(1/T_{2,i}^*|t, \rho). \quad (1)$$

The MLE procedure determines what coherence distribution best predicts the measured distribution in Fig. 4(c). In Fig. 5(a), we plot $L(t, \rho)$ over the computational phase space for the coherence times in Fig. 4(c). We find a band of potential bath geometries that satisfy the observed coherence time distribution rather than uniquely predicting a single set of values. Based on the CVD growth discussed in Sec. IV B,

we estimate the bath thickness at $t_{\mathrm{SIMS}} = 4\,\mathrm{nm}$ and plot the line cut of L in Fig. 5(b). This provides a measure of the bath density of $4.1 \pm .8\,\mathrm{ppm}$, where the error is found by fitting $L(t_{\mathrm{SIMS}}, \rho)$ to a normal distribution. This density estimation is not sensitive to the variation in SIMS measurements discussed in Sec. II B.

We benchmark the error in the MLE procedure versus the number of coherence time samples in Fig. 5(c). For each number of samples N and set of bath parameters, 200 random T_2^* data sets of N coherence times are chosen from the numerical data sets used in Sec. II. Then, the likelihood is calculated for a fixed thickness t_0, and the relative error for one data set is calculated as $\epsilon^2_{\rho_0} = (\rho_{\mathrm{MLE}} - \rho_0)^2/\rho_0^2$, where ρ_{MLE} is the density such that $L(t_0, \rho_{\mathrm{MLE}}) = \max[L(t_0, \rho)]$. This is averaged over a range of tested densities, plotted in Fig. 5(c). We calculate the error for eight samples to be 25 %, corresponding to an uncertainty of 0.9 ppm for the density estimate from Fig. 5(a). This is similar to the error from fitting L and is stable when the thickness is varied. We fit the average error as AN^{-p}, shown over the calculated error in Fig. 5(c), finding a $N^{-0.55}$ trend.

In Fig. 5(d), we explore the addition of more complex coherence measurements to the MLE procedure. Making use of simulated Hahn-echo and Ramsey coherence times for four NV centers chosen randomly from the 3-nm-thick, 5-ppm spin bath computational data set in Fig. 3, we perform MLE with just Hahn-echo times (left) and just Ramsey times (center), as well as the joint probability of both data sets. We find that the combined set more precisely predicts both bath density and thickness compared to the individual data sets, suggesting that incorporating more time-expensive (both computationally and experimentally) coherence measurements may remove the need for *ex situ* growth characterization.

F. Strong coupling yield

Entangled qubit-based sensors promise to greatly enhance quantum sensing capabilities as compared to the current state of the art [24,25]. The applicability of these schemes is enabled by the high-yield synthesis of strongly coupled quantum systems (NV center spins and multiple single bath spins). We consider the impact of growth dimensionality on the yield of such systems analytically, quantifying our results with numerical predictions. In our calculations we consider central NV center spins and P1 center bath spins, but our approach is easily generalized to other spin systems.

Each bath spin couples to the NV center with a dipolar coupling strength A_z^i. The NV center coherence in the absence of dynamical protocols and coupled to a bath of many weakly coupled spins can be described as a product of individual coupling contributions (see Methods).

We aim to describe how likely the coupling to the nearest spin, A_0, is to be greater than the dephasing from the rest of the bath A_{bath}. The distributions of nearest-neighbor distance r_{NN} in two and three dimensions are

$$g_{2\mathrm{D}} = \exp\left(-\pi r_{\mathrm{NN}}^2 \varsigma\right)\varsigma\, 2\pi r_{\mathrm{NN}}, \tag{2}$$

$$g_{3\mathrm{D}} = \exp\left(-4\pi r_{\mathrm{NN}}^3 \rho/3\right)\rho\, 4\pi r_{\mathrm{NN}}^2, \tag{3}$$

where ρ is the 3D density and $\varsigma = \rho t$ is the 2D density for bath thickness t nominally less than the average nearest-neighbor distance. Notably, the distributions depend on the bath dimensionality. The bath decoherence can be estimated as follows:

$$\Gamma_{2\mathrm{D}}^{\mathrm{bath}} \propto \sqrt{\sum_{2\mathrm{D}} |1/r^3|^2} = \sqrt{\int_0^\infty dr\, 2\pi r \varsigma r^{-6}}, \tag{4}$$

$$\Gamma_{3\mathrm{D}}^{\mathrm{bath}} \propto \sqrt{\sum_{3\mathrm{D}} |1/r^3|^2} = \sqrt{\int_0^\infty dr\, 4\pi r^2 \rho r^{-6}}. \tag{5}$$

We now define the visibility ν of the nearest-neighbor spin as a ratio between its coupling to the central spin A_0 and the decoherence rate induced by all other spins A_{bath},

$$\nu = \frac{|A_0|}{\sqrt{2}A_{\mathrm{bath}}}, \tag{6}$$

and average ν over many bath configurations. Assuming the point dipole approximation to compute the coupling between central and bath spins, we find the average visibility at the given dimensionality as $\langle \nu_{k\mathrm{D}} \rangle = \langle |A_0|/\sqrt{2}A_{\mathrm{bath}} \rangle \simeq \langle r_{\mathrm{NN}}^{-3}/\sqrt{2}\Gamma_{k\mathrm{D}} \rangle$, where $\Gamma_{k\mathrm{D}}$ ($k = \{2, 3\}$) are given by Eqs. (4) and (5). We note here that averaging $\Gamma_{k\mathrm{D}}$ assumes the dephasing rate due to the rest of the spin bath follows a highly peaked distribution. We then ask if this average is larger for lower-dimensional spin baths by evaluating

$$\frac{\nu_{2\mathrm{D}}}{\nu_{3\mathrm{D}}} = \frac{\langle r_{\mathrm{NN}}^{-3}/\Gamma_{2\mathrm{D}} \rangle}{\langle r_{\mathrm{NN}}^{-3}/\Gamma_{3\mathrm{D}} \rangle} = \sqrt{2}. \tag{7}$$

We find that the visibility of the nearest-neighbor spin is $\sqrt{2}$ larger in the 2D case, pointing to the fact that the yield of strongly coupled bath spins is significantly higher in low-dimensional systems.

We confirm these analytical predictions with numerical simulations. Using the PyCCE code, we generate 10^5 50-nm-thick P1 electron spin baths in a (001)-oriented diamond lattice whose densities range over two orders of magnitude and divide each bath into slices of varying thickness. For each density and thickness, we compute visibility ν [Eq. (6)]. Representative histograms for 3-ppm spin baths are shown in Fig. 6(a). As the bath thickness decreases, the visibility distribution shifts to higher values, in line with the prediction from Eq. (7). We follow the criterion laid out in the Methods and Eq. (11) below to identify strongly coupled bath spins. We set a threshold for the visibility at $\nu \geqslant 2\pi$. At this value, coherence goes through a full oscillation period when the signal contrast reaches $1/e$.

We plot the resulting probability of obtaining strongly coupled spins in Fig. 6(b) for each density. At all densities, the likelihood of finding a NV spin bath configuration with the desired coupling ratio is almost three times higher in the thin bath limit. Furthermore, there is a crossover transition for each density from three-dimensional to two-dimensional behavior, which intersects with the average nearest-neighbor spacing $\langle r_{\mathrm{NN}} \rangle = 0.554\rho^{-1/3}$, obtained from Eq. (3). Heuristically, as the thickness reduces below $\langle r_{\mathrm{NN}} \rangle$, there are no spins proximal to the central spin in the out-of-plane direction, only in the plane of the central spin.

In Fig. 6(c) we further corroborate the analytical result from Eq. (7). We plot the visibility probability distributions

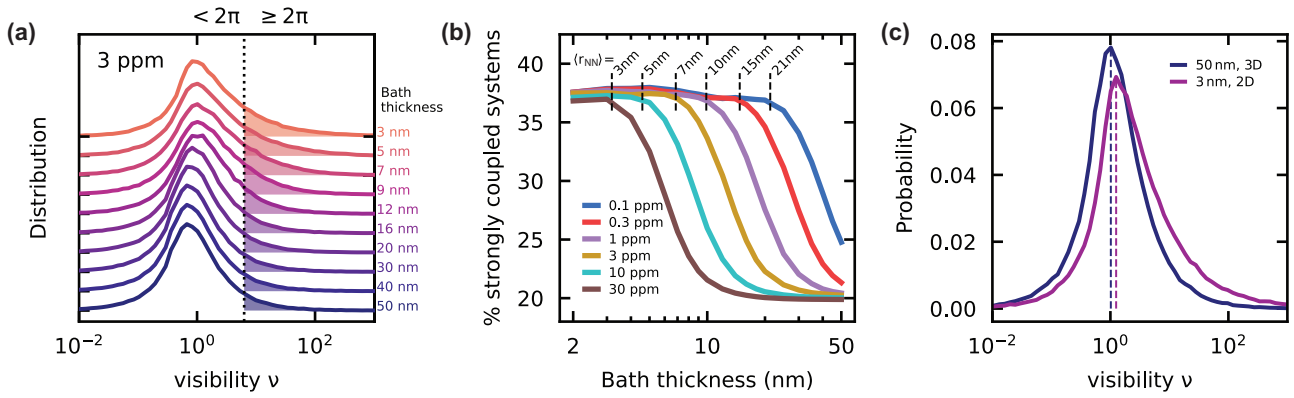

FIG. 6. Dimensionality dependence of strong coupling. (a) Computed distribution (using PyCCE) of ratio of nearest-neighbor P1 coupling to background decoherence rate for 10^5 3 ppm density P1 bath configurations with varying thickness. Curves are offset for clarity. Shaded regions right of the dashed line indicate $\nu \geqslant 2\pi$. (b) Percentage of NV-P1 bath systems with at least one strongly coupled bath spin for varying bath density and thickness. The average spin-spin distance is marked atop curves for each density. (c) Calculated visibility distributions for 3D and 2D spin baths (solid lines), with most likely values shown with dashed lines.

for a 3-ppm bath in the 3D (50 nm) and 2D (3 nm) limit (solid lines), with the peak values (most likely values) shown in dashed lines. The ratio of the most likely values is $\nu_{2D,peak}/\nu_{3D,peak} = 1.23$, in agreement with the value extracted in Eq. (7).

III. OUTLOOK

Point defects in diamond and other wide-band-gap semiconductors are promising platforms for qubit-based sensors. Deterministic synthesis of such systems will benefit from feed-forward techniques that optimize host crystal parameters for specific outcomes and applications. Additionally, such systems pave the way for entangled qubit-based sensors, which hold great promise to enhance current quantum sensing capabilities. In this paper, we have demonstrated holistic quantum simulations of NV center coherence, with techniques applicable to other spin defects, as a tool for quantum system coherence characterization driven synthesis, minimizing the need for large-scale and destructive materials characterization. Practically, we showed how our approach allows for the use of rudimentary T_2^* measurements to approximate *in situ* doping densities, even with little prior sample knowledge. Specifically, we have demonstrated a MLE model based on a CCE-generated distribution library as an aid to process calibration and sample characterization. This method is nondestructive and operates at the density scales relevant for quantum technologies.

Additionally, the coherence distribution results presented in this paper explore the expected sample properties in low-dimensional spin baths. By going beyond approximate analytical treatments and sampling over a wide distribution of random bath configurations with a range of central spin bath couplings, the CCE calculations quantitatively capture the connection between bath geometries and coherence time distributions, providing an invaluable analytical tool for experimental design.

While in this work we focus on a single dominant spin bath species in low-dimensional geometries, our MLE method is not limited to this regime. CCE methods can readily be extended to additional spin bath species in diamond, as well as mixed nuclear and electronic spin baths. By calculating coherence times in these other situations, dopant densities in samples with multiple dominant noise sources can be characterized. Furthermore, the strategy presented here can be applied to other solid-state hosts where qubit coherence is limited by spin bath noise.

IV. METHODS

Our work builds on two previously established techniques, CCE calculations [66,67] and PECVD synthesis of NV centers in diamond [41], as described below and in Fig. 2. We focus on the ^{15}N isotope of nitrogen for the majority of the calculations as this allows us to experimentally distinguish intentionally doped defects from background occurring defects [29,41]. In all calculations and measurements the external magnetic field is aligned along the crystal-field axis of the NV centers.

A. Theory

The dynamics of the system are simulated using the following Hamiltonian:

$$\hat{H} = -\gamma_e B_z \hat{S}_z + D\hat{S}_z^2 + \sum_i a(m_i)\hat{P}_{z,i} - \gamma_e B_z \hat{P}_{z,i} + \sum_i \mathbf{S}\mathbf{A}^i\mathbf{P}_i + \sum_{i\neq j} \mathbf{P}_i\mathbf{J}^{ij}\mathbf{P}_j, \quad (8)$$

where γ_e is the electron spin gyromagnetic ratio, B_z is the magnetic field aligned with the z axis, $\mathbf{S} = (\hat{S}_x, \hat{S}_y, \hat{S}_z)$ are NV center spin operators, D is the NV zero-field splitting, $\mathbf{P} = (\hat{P}_x, \hat{P}_y, \hat{P}_z)$ are spin operators of the P1 center, and $a(m_i)$ is the hyperfine coupling between the P1 ^{15}N nuclear spin and the P1 electron spin, dependent on the random orientation of the Jahn-Teller axis along one of four crystal directions and the nuclear spin state for each P1 (m_i), where i runs over all the simulated P1 centers [70]. $\mathbf{A}^i$ are dipolar couplings between the NV center and P1 centers, and $\mathbf{J}^{ij}$ is the coupling between

two P1 electron spins. The applied 50 G is sufficiently past the high-field limit, and these calculations translate over to measurements at higher fields as well (see Supplemental Material, Sec. S.I.A [68]).

In the Supplemental Material (Secs. S.I.B and S.I.C) [68], we show convergence tests for Ramsey and Hahn-echo simulations versus both CCE order (1 and 4, respectively) and total number of simulated bath spins. We use CCE methods with bath state sampling [71] to achieve convergence for the electron spin bath. For each pure electron bath state the state of ^{15}N spin and the P1 crystallographic orientation is chosen at random. At each set of bath parameters, the nitrogen density is taken to be spatially uniform throughout the doped layer, with local inhomogeneity introduced by randomly generating the spin distribution. More details about the method are available in [60].

The CCE approach [66,67] approximates the coherence function $\mathcal{L}(t) = \frac{\langle \sigma_-(t)\rangle}{\langle \sigma_-(0)\rangle} = \frac{\langle 0|\hat{\rho}(t)|1\rangle}{\langle 0|\hat{\rho}(0)|1\rangle}$, the normalized off-diagonal element of the density matrix $\rho_{m,n}$ of the qubit, where m and n are either the ground or excited spin states $|0\rangle$ and $|1\rangle$, respectively. $\mathcal{L}(t)$ is approximated as a product of cluster contributions:

$$\mathcal{L}(t) = \prod_i \tilde{L}^{\{i\}} \prod_{i,j} \tilde{L}^{\{ij\}} \ldots, \tag{9}$$

where $\tilde{L}^{\{i\}}$ is the contribution of a single bath spin, $\tilde{L}^{\{ij\}}$ is the contribution of spin pairs, and so on for higher-order clusters [Fig. 2(a)]. The maximum size of the cluster n included in the expansion denotes the order of CCEn approximation.

The Ramsey signal is converged at the first order of CCE. As such, we can represent the high-field Ramsey coherence function in the rotating frame for a bath in a fully mixed state as [72]

$$\begin{aligned}\mathcal{L}(t) &\approx \prod_j^N \cos\frac{A_z^j t}{2} \approx \exp\left[-\frac{A_{\text{bath}}^2}{2}t^2\right]\prod_i^n \cos\frac{A_z^i t}{2} \\ &= \exp\left[-\left(\frac{t}{T_2^*}\right)^2\right]\prod_i^n \cos\frac{A_z^i t}{2},\end{aligned} \tag{10}$$

where $A_{\text{bath}}^2 = \frac{\sum_j (A_z^j)^2}{4}$, $T_2^* = \frac{\sqrt{2}}{A_{\text{bath}}}$, index i goes over only n strongly coupled P1 centers, and index j goes over all other P1s. We define strongly coupled bath spins as those distinguishable from the background decoherence, setting a threshold for its visibility [Eq. (6)] as

$$\nu_i = \frac{|A_z^i|}{2} \geqslant 2\pi\frac{A_{\text{bath}}}{\sqrt{2}}, \tag{11}$$

so that at least one full period of oscillation of the coherence function is visible when the signal contrast reaches $1/e$. For each random bath configuration, we order the P1 spins by the strength of the coupling and one by one select out the strongly coupled spins until the condition (11) is violated. T_2^* is then recovered from the coupling to the remaining bath spins.

Reference [58] shows that CCE at second order can be used to qualitatively recover the behavior of T_2 coherence times in the P1 bath. We further extend this approach and converge CCE Hahn-echo calculations at fourth order with bath-state sampling [see Supplemental Material, Sec. S.I.B and Fig. S1(c) [68]].

B. Materials growth

All defects studied in this work are doped *in situ* during diamond PECVD with subsequent electron irradiation and annealing for NV center activation. This recipe constitutes our standard PECVD process for growing isotopically pure diamond with isotopically tagged NV centers, as shown in Fig. 2(d). High-purity electronic grade ($\leqslant$ 10 ppb) diamond substrates 2 mm by 2 mm by 0.5 mm, with ⟨001⟩ growth face and ⟨110⟩ sides (element six) were used as starting substrates. The as-received substrates were Chemical-Mechanical Polished (CMP) to a surface roughness of $R_q \leqslant 0.4$ nm by Syntek, LLC. Subsequently, these substrates were inductively coupled plasma reactive ion etched (ICP-RIE) down to remove ≈2.5 μm of damaged diamond surface using a composite, cycled Ar/Cl_2 and O_2 plasma etching recipe. Pregrowth, the samples were annealed at 1200 °C and triacid cleaned to mobilize/annihilate vacancy clusters and remove any amorphous/sp^2 carbon, respectively. See Supplemental Material, Sec. S.II, for a more detailed description of sample processing [68].

Homoepitaxial growth of diamond was performed in a custom-configured PECVD reactor [73] (Seki Diamond). The growth chamber was pumped down to 8×10^{-8} Torr to minimize background contamination. Thereafter, high-purity H_2 (99.99999%) was introduced into the chamber, with the process microwave power of 11.5 W mm^{-2} and pressure of 25 Torr maintained throughout. The substrate temperature was maintained in the range of 800 ± 27 °C as tracked by an IR pyrometer. Before introduction of the diamond growth precursor, the sample was submitted to a H_2 and O_2 etch (4% of O_2) for 5 min and a subsequent 20-min etch using H_2 only, to etch away any residual surface contaminants and defects, and expose the growth surface atomic step edges [38,74]. Thereafter, $^{12}CH_4$ (99.9999% chemical purity, 99.99 at.% isotopic purity) is introduced as the carbon precursor. The methane-to-hydrogen ratio is maintained constant at 0.1 % (H_2:$^{12}CH_4$ = 400 sccm : 0.4 sccm) as to ensure step-flow growth [38,73]. After CVD growth is completed and the plasma is turned off, the sample is vacuum-annealed in the growth chamber at a pressure of $\leqslant 1\times10^{-6}$ Torr and temperature of 500–600 °C for 3-h to out-gas hydrogen contaminants prior to NV center synthesis. Growth rates for the obtained films were determined to be 38 ± 10 nm h^{-1} via *ex situ* secondary ion mass spectrometry (SIMS) analysis averaged over six calibration substrates [e.g., ^{12}C overgrowth shown in Fig. 2(e)].

Postgrowth, bulk electron irradiation with a 2×10^{14} cm^{-2} dose at 2 MeV and a 2-h anneal at 850 °C under an Ar atmosphere converts a fraction of doped nitrogen into NV centers with [^{15}NV] ≈ 0.01 ppb to 0.1 ppb, with the remaining nitrogen sites persisting as N_s (P1 centers). NV activation is intentionally performed in a vacancy diffusion-limited regime [42] in order to reliably obtain optically resolvable single NV centers. As the nitrogen doping is buried 50 nm below the diamond surface, we do not expect band-bending effects on the defect charge states [75,76].

The data that support the findings of this study are available from the corresponding author upon reasonable request.

ACKNOWLEDGMENTS

This work was primarily supported by the U.S. Department of Energy, Office of Science, Basic Energy Sciences, Materials Sciences and Engineering Division (J.C.M., F.J.H., N.D., D.D.A.) and the Design and Optimization of Synthesizable Materials with Targeted Quantum Characteristics (Grant No. AFOSRFA9550-22-1-0370). We acknowledge additional support from Midwest Integrated Center for Computational Materials (MICCoM) as part of the Computational Materials Sciences Program funded by the U.S. Department of Energy (M.O. and G.G.), the Q-NEXT Quantum Center as part of the U.S. Department of Energy, Office of Science, National Quantum Information Science Research Centers (M.F.), and the Center for Novel Pathways to Quantum Coherence in Materials, an Energy Frontier Research Center funded by the U.S. Department of Energy, Office of Science, Basic Energy Sciences (Y.-X.W.). J.C.M. acknowledges prior support from the National Science Foundation Graduate Research Fellowship Program (Grant No. DGE-1746045). M.O. acknowledges the support from the Google Ph.D. Fellowship. M.W. acknowledges support from the GEM Fellowship Program. This work made use of the Pritzker Nanofabrication Facility of the Institute for Molecular Engineering at the University of Chicago, which receives support from Soft and Hybrid Nanotechnology Experimental (SHyNE) Resource (NSF Grant No. ECCS-2025633), a node of the National Science Foundation's National Nanotechnology Coordinated Infrastructure. This work made use of the shared facilities at the University of Chicago Materials Research Science and Engineering Center, supported by the National Science Foundation under Award No. DMR-2011854.

J.C.M. and M.O. conceived the study and contributed equally to this work. J.C.M. performed experimental measurements and analyzed the data. M.O. performed theoretical simulations. N.D. grew the diamond sample and analyzed SIMS results. Y.-X.W. and M.F. helped develop the MLE and strong coupling models. M.W. assisted in conducting simulations. D.D.A, G.G., F.J.H., and A.A.C. advised on all efforts. All authors contributed to writing the manuscript.

The work described here is the basis of a patent application that is pending with the USPTO, filed by authors J.C.M., M.O., Y.-X.W., M.F., N.D., F.J.H., A.A.C., G.G., and D.D.A.

[1] M. W. Doherty, N. B. Manson, P. Delaney, F. Jelezko, J. Wrachtrup, and L. C. Hollenberg, The nitrogen-vacancy colour centre in diamond, Phys. Rep. **528**, 1 (2013).

[2] C. Bradac, W. Gao, J. Forneris, M. E. Trusheim, and I. Aharonovich, Quantum nanophotonics with group iv defects in diamond, Nat. Commun. **10**, 5625 (2019).

[3] G. Balasubramanian, I. Y. Chan, R. Kolesov, M. Al-Hmoud, J. Tisler, C. Shin, C. Kim, A. Wojcik, P. R. Hemmer, A. Krueger, T. Hanke, A. Leitenstorfer, R. Bratschitsch, F. Jelezko, and J. Wrachtrup, Nanoscale imaging magnetometry with diamond spins under ambient conditions, Nature (London) **455**, 648 (2008).

[4] J. R. Maze, P. L. Stanwix, J. S. Hodges, S. Hong, J. M. Taylor, P. Cappellaro, L. Jiang, M. V. G. Dutt, E. Togan, A. S. Zibrov, A. Yacoby, R. L. Walsworth, and M. D. Lukin, Nanoscale magnetic sensing with an individual electronic spin in diamond, Nature (London) **455**, 644 (2008).

[5] B. J. Maertz, A. P. Wijnheijmer, G. D. Fuchs, M. E. Nowakowski, and D. D. Awschalom, Vector magnetic field microscopy using nitrogen vacancy centers in diamond, Appl. Phys. Lett. **96**, 092504 (2010).

[6] D. L. Sage, K. Arai, D. R. Glenn, S. J. DeVience, L. M. Pham, L. Rahn-Lee, M. D. Lukin, A. Yacoby, A. Komeili, and R. L. Walsworth, Optical magnetic imaging of living cells, Nature (London) **496**, 486 (2013).

[7] L. Rondin, J.-P. Tetienne, T. Hingant, J.-F. Roch, P. Maletinsky, and V. Jacques, Magnetometry with nitrogen-vacancy defects in diamond, Rep. Prog. Phys. **77**, 056503 (2014).

[8] H. J. Mamin, M. Kim, M. H. Sherwood, C. T. Rettner, K. Ohno, D. D. Awschalom, and D. Rugar, Nanoscale nuclear magnetic resonance with a nitrogen-vacancy spin sensor, Science **339**, 557 (2013).

[9] T. Staudacher, F. Shi, S. Pezzagna, J. Meijer, J. Du, C. A. Meriles, F. Reinhard, and J. Wrachtrup, Nuclear magnetic resonance spectroscopy on a (5-nanometer)^3 sample volume, Science **339**, 561 (2013).

[10] F. Casola, T. van der Sar, and A. Yacoby, Probing condensed matter physics with magnetometry based on nitrogen-vacancy centres in diamond, Nat. Rev. Mater. **3**, 17088 (2018).

[11] Z. Zhao, X. Ye, S. Xu, P. Yu, Z. Yang, X. Kong, Y. Wang, T. Xie, F. Shi, and J. Du, Sub-nanotesla sensitivity at the nanoscale with a single spin, Natl. Sci. Rev. **10**, nwad100 (2023).

[12] N. Kalb, A. A. Reiserer, P. C. Humphreys, J. J. W. Bakermans, S. J. Kamerling, N. H. Nickerson, S. C. Benjamin, D. J. Twitchen, M. Markham, and R. Hanson, Entanglement distillation between solid-state quantum network nodes, Science **356**, 928 (2017).

[13] C. T. Nguyen, D. D. Sukachev, M. K. Bhaskar, B. Machielse, D. S. Levonian, E. N. Knall, P. Stroganov, R. Riedinger, H. Park, M. Lončar, and M. D. Lukin, Quantum network nodes based on diamond qubits with an efficient nanophotonic interface, Phys. Rev. Lett. **123**, 183602 (2019).

[14] C. T. Nguyen, D. D. Sukachev, M. K. Bhaskar, B. Machielse, D. S. Levonian, E. N. Knall, P. Stroganov, C. Chia, M. J. Burek, R. Riedinger, H. Park, M. Lončar, and M. D. Lukin, An integrated nanophotonic quantum register based on silicon-vacancy spins in diamond, Phys. Rev. B **100**, 165428 (2019).

[15] M. Pompili, S. L. N. Hermans, S. Baier, H. K. C. Beukers, P. C. Humphreys, R. N. Schouten, R. F. L. Vermeulen, M. J. Tiggelman, L. dos Santos Martins, B. Dirkse, S. Wehner, and R. Hanson, Realization of a multinode quantum network of remote solid-state qubits, Science **372**, 259 (2021).

[16] S. L. N. Hermans, M. Pompili, H. K. C. Beukers, S. Baier, J. Borregaard, and R. Hanson, Qubit teleportation between non-neighbouring nodes in a quantum network, Nature (London) **605**, 663 (2022).

[17] D. M. Toyli, D. J. Christle, A. Alkauskas, B. B. Buckley, C. G. V. de Walle, and D. D. Awschalom, Measurement and

control of single nitrogen-vacancy center spins above 600 k, Phys. Rev. X **2**, 031001 (2012).

[18] G.-Q. Liu, X. Feng, N. Wang, Q. Li, and R.-B. Liu, Coherent quantum control of nitrogen-vacancy center spins near 1000 kelvin, Nat. Commun. **10**, 1344 (2019).

[19] F. J. Heremans, C. G. Yale, and D. D. Awschalom, Control of spin defects in wide-bandgap semiconductors for quantum technologies, Proc. IEEE **104**, 2009 (2016).

[20] M. Pfender, N. Aslam, H. Sumiya, S. Onoda, P. Neumann, J. Isoya, C. A. Meriles, and J. Wrachtrup, Nonvolatile nuclear spin memory enables sensor-unlimited nanoscale spectroscopy of small spin clusters, Nat. Commun. **8**, 834 (2017).

[21] C. E. Bradley, J. Randall, M. H. Abobeih, R. C. Berrevoets, M. J. Degen, M. A. Bakker, M. Markham, D. J. Twitchen, and T. H. Taminiau, A ten-qubit solid-state spin register with quantum memory up to one minute, Phys. Rev. X **9**, 031045 (2019).

[22] M. J. Degen, S. J. Loenen, H. P. Bartling, C. E. Bradley, A. L. Meinsma, M. Markham, D. J. Twitchen, and T. H. Taminiau, Entanglement of dark electron-nuclear spin defects in diamond, Nat. Commun. **12**, 3470 (2021).

[23] T. Xie, Z. Zhao, X. Kong, W. Ma, M. Wang, X. Ye, P. Yu, Z. Yang, S. Xu, P. Wang, Y. Wang, F. Shi, and J. Du, Beating the standard quantum limit under ambient conditions with solid-state spins, Sci. Adv. **7**, eabg9204 (2021).

[24] T.-X. Zheng, A. Li, J. Rosen, S. Zhou, M. Koppenhöfer, Z. Ma, F. T. Chong, A. A. Clerk, L. Jiang, and P. C. Maurer, Preparation of metrological states in dipolar-interacting spin systems, npj Quantum Inf. **8**, 150 (2022).

[25] C. A. Meriles, P. R. Zangara, and D. Pagliero, Quantum Sensing via Magnetic-Noise-Protected States in an Electronic Spin Dyad, Adv. Quantum Technol. 2300098 (2023).

[26] R. Hanson, F. M. Mendoza, R. J. Epstein, and D. D. Awschalom, Polarization and readout of coupled single spins in diamond, Phys. Rev. Lett. **97**, 087601 (2006).

[27] H. S. Knowles, D. M. Kara, and M. Atatüre, Demonstration of a coherent electronic spin cluster in diamond, Phys. Rev. Lett. **117**, 100802 (2016).

[28] J. Meijer, B. Burchard, M. Domhan, C. Wittmann, T. Gaebel, I. Popa, F. Jelezko, and J. Wrachtrup, Generation of single color centers by focused nitrogen implantation, Appl. Phys. Lett. **87**, 261909 (2005).

[29] J. R. Rabeau, P. Reichart, G. Tamanyan, D. N. Jamieson, S. Prawer, F. Jelezko, T. Gaebel, I. Popa, M. Domhan, and J. Wrachtrup, Implantation of labelled single nitrogen vacancy centers in diamond using ^{15}N, Appl. Phys. Lett. **88**, 023113 (2006).

[30] T. Gaebel, M. Domhan, I. Popa, C. Wittmann, P. Neumann, F. Jelezko, J. R. Rabeau, N. Stavrias, A. D. Greentree, S. Prawer, J. Meijer, J. Twamley, P. R. Hemmer, and J. Wrachtrup, Room-temperature coherent coupling of single spins in diamond, Nat. Phys. **2**, 408 (2006).

[31] P. Neumann, R. Kolesov, B. Naydenov, J. Beck, F. Rempp, M. Steiner, V. Jacques, G. Balasubramanian, M. L. Markham, D. J. Twitchen, S. Pezzagna, J. Meijer, J. Twamley, F. Jelezko, and J. Wrachtrup, Quantum register based on coupled electron spins in a room-temperature solid, Nat. Phys. **6**, 249 (2010).

[32] F. Dolde, I. Jakobi, B. Naydenov, N. Zhao, S. Pezzagna, C. Trautmann, J. Meijer, P. Neumann, F. Jelezko, and J. Wrachtrup, Room-temperature entanglement between single defect spins in diamond, Nat. Phys. **9**, 139 (2013).

[33] E. L. Rosenfeld, L. M. Pham, M. D. Lukin, and R. L. Walsworth, Sensing coherent dynamics of electronic spin clusters in solids, Phys. Rev. Lett. **120**, 243604 (2018).

[34] A. Cooper, W. K. C. Sun, J. C. Jaskula, and P. Cappellaro, Identification and control of electron-nuclear spin defects in diamond, Phys. Rev. Lett. **124**, 083602 (2020).

[35] J. Lee, M. Tatsuta, A. Xu, E. Bauch, M. J. H. Ku, and R. L. Walsworth, Dressed-state control of effective dipolar interaction between strongly-coupled solid-state spins, npj Quantum Inf. **9**, 77 (2023).

[36] T. Yamamoto, T. Umeda, K. Watanabe, S. Onoda, M. L. Markham, D. J. Twitchen, B. Naydenov, L. P. McGuinness, T. Teraji, S. Koizumi, F. Dolde, H. Fedder, J. Honert, J. Wrachtrup, T. Ohshima, F. Jelezko, and J. Isoya, Extending spin coherence times of diamond qubits by high-temperature annealing, Phys. Rev. B **88**, 075206 (2013).

[37] H. Okushi, H. Watanabe, S. Ri, S. Yamanaka, and D. Takeuchi, Device-grade homoepitaxial diamond film growth, J. Cryst. Growth **237–239**, 1269 (2002).

[38] K. Ohno, Nanometer-scale engineering of shallow spins in diamond, Ph.D. thesis, University of California, Santa Barbara, 2014.

[39] T. R. Eichhorn, C. A. McLellan, and A. C. B. Jayich, Optimizing the formation of depth-confined nitrogen vacancy center spin ensembles in diamond for quantum sensing, Phys. Rev. Mater. **3**, 113802 (2019).

[40] P. Balasubramanian, C. Osterkamp, O. Brinza, M. Rollo, I. Robert-Philip, P. Goldner, V. Jacques, F. Jelezko, J. Achard, and A. Tallaire, Enhancement of the creation yield of NV ensembles in a chemically vapour deposited diamond, Carbon **194**, 282 (2022).

[41] K. Ohno, F. J. Heremans, L. C. Bassett, B. A. Myers, D. M. Toyli, A. C. B. Jayich, C. J. Palmstrøm, and D. D. Awschalom, Engineering shallow spins in diamond with nitrogen delta-doping, Appl. Phys. Lett. **101**, 082413 (2012).

[42] K. Ohno, F. J. Heremans, C. F. D. L. Casas, B. A. Myers, B. J. Alemán, A. C. B. Jayich, and D. D. Awschalom, Three-dimensional localization of spins in diamond using ^{12}C implantation, Appl. Phys. Lett. **105**, 052406 (2014).

[43] C. A. McLellan, B. A. Myers, S. Kraemer, K. Ohno, D. D. Awschalom, and A. C. B. Jayich, Patterned formation of highly coherent nitrogen-vacancy centers using a focused electron irradiation technique, Nano Lett. **16**, 2450 (2016).

[44] D. M. Toyli, C. D. Weis, G. D. Fuchs, T. Schenkel, and D. D. Awschalom, Chip-scale nanofabrication of single spins and spin arrays in diamond, Nano Lett. **10**, 3168 (2010).

[45] P. Spinicelli, A. Dréau, L. Rondin, F. Silva, J. Achard, S. Xavier, S. Bansropun, T. Debuisschert, S. Pezzagna, J. Meijer, V. Jacques, and J. F. Roch, Engineered arrays of nitrogen-vacancy color centers in diamond based on implantation of cn$^-$ molecules through nanoapertures, New J. Phys. **13**, 025014 (2011).

[46] S. Sangtawesin, T. O. Brundage, Z. J. Atkins, and J. R. Petta, Highly tunable formation of nitrogen-vacancy centers via ion implantation, Appl. Phys. Lett. **105**, 063107 (2014).

[47] I. Jakobi, S. A. Momenzadeh, F. F. D. Oliveira, J. Michl, F. Ziem, M. Schreck, P. Neumann, A. Denisenko, and J. Wrachtrup, *Efficient Creation of Dipolar Coupled*

Nitrogen-Vacancy Spin Qubits in Diamond (Institute of Physics Publishing, Bristol, 2016), p. 012001.

[48] I. Bayn, E. H. Chen, M. E. Trusheim, L. Li, T. Schröder, O. Gaathon, M. Lu, A. Stein, M. Liu, K. Kisslinger, H. Clevenson, and D. Englund, Generation of ensembles of individually resolvable nitrogen vacancies using nanometer-scale apertures in ultrahigh-aspect ratio planar implantation masks, Nano Lett. **15**, 1751 (2015).

[49] T.-Y. Hwang, J. Lee, S.-W. Jeon, Y.-S. Kim, Y.-W. Cho, H.-T. Lim, S. Moon, S.-W. Han, Y.-H. Choa, and H. Jung, Sub-10 nm precision engineering of solid-state defects via nanoscale aperture array mask, Nano Lett. **22**, 1672 (2022).

[50] N. Mizuochi, P. Neumann, F. Rempp, J. Beck, V. Jacques, P. Siyushev, K. Nakamura, D. J. Twitchen, H. Watanabe, S. Yamasaki, F. Jelezko, and J. Wrachtrup, Coherence of single spins coupled to a nuclear spin bath of varying density, Phys. Rev. B **80**, 041201(R) (2009).

[51] G. Balasubramanian, P. Neumann, D. Twitchen, M. Markham, R. Kolesov, N. Mizuochi, J. Isoya, J. Achard, J. Beck, J. Tissler, V. Jacques, P. R. Hemmer, F. Jelezko, and J. Wrachtrup, Ultralong spin coherence time in isotopically engineered diamond, Nat. Mater. **8**, 383 (2009).

[52] E. J. Davis, B. Ye, F. Machado, S. A. Meynell, W. Wu, T. Mittiga, W. Schenken, M. Joos, B. Kobrin, Y. Lyu, Z. Wang, D. Bluvstein, S. Choi, C. Zu, A. C. B. Jayich, and N. Y. Yao, Probing many-body dynamics in a two-dimensional dipolar spin ensemble, Nat. Phys. **19**, 836 (2023).

[53] L. B. Hughes, Z. Zhang, C. Jin, S. A. Meynell, B. Ye, W. Wu, Z. Wang, E. J. Davis, T. E. Mates, N. Y. Yao, K. Mukherjee, and A. C. Bleszynski Jayich, Two-dimensional spin systems in pecvd-grown diamond with tunable density and long coherence for enhanced quantum sensing and simulation, APL Mater. **11**, 021101 (2023).

[54] T. Lühmann, R. John, R. Wunderlich, J. Meijer, and S. Pezzagna, Coulomb-driven single defect engineering for scalable qubits and spin sensors in diamond, Nat. Commun. **10**, 4956 (2019).

[55] E. D. Herbschleb, H. Kato, Y. Maruyama, T. Danjo, T. Makino, S. Yamasaki, I. Ohki, K. Hayashi, H. Morishita, M. Fujiwara, and N. Mizuochi, Ultra-long coherence times amongst room-temperature solid-state spins, Nat. Commun. **10**, 3766 (2019).

[56] R. Kawase, H. Kawashima, H. Kato, N. Tokuda, S. Yamasaki, M. Ogura, T. Makino, and N. Mizuochi, *n*-type diamond synthesized with tert-butylphosphine for long spin coherence times of perfectly aligned NV centers, J. Appl. Phys. **132**, 174504 (2022).

[57] E. Bauch, S. Singh, J. Lee, C. A. Hart, J. M. Schloss, M. J. Turner, J. F. Barry, L. M. Pham, N. Bar-Gill, S. F. Yelin, and R. L. Walsworth, Decoherence of ensembles of nitrogen-vacancy centers in diamond, Phys. Rev. B **102**, 134210 (2020).

[58] H. Park, J. Lee, S. Han, S. Oh, and H. Seo, Decoherence of nitrogen-vacancy spin ensembles in a nitrogen electron-nuclear spin bath in diamond, npj Quantum Inf. **8**, 95 (2022).

[59] M. Onizhuk and G. Galli, Substrate-controlled dynamics of spin qubits in low dimensional van der waals materials, Appl. Phys. Lett. **118**, 154003 (2021).

[60] M. Onizhuk and G. Galli, Pycce: A python package for cluster correlation expansion simulations of spin qubit dynamics, Adv. Theory Simul. **4**, 2100254 (2021).

[61] S. Kanai, F. J. Heremans, H. Seo, G. Wolfowicz, C. P. Anderson, S. E. Sullivan, M. Onizhuk, G. Galli, D. D. Awschalom, and H. Ohno, Generalized scaling of spin qubit coherence in over 12,000 host materials, Proc. Natl. Acad. Sci. USA **119**, e2121808119 (2022).

[62] S. L. Bayliss, P. Deb, D. W. Laorenza, M. Onizhuk, G. Galli, D. E. Freedman, and D. D. Awschalom, Enhancing spin coherence in optically addressable molecular qubits through host-matrix control, Phys. Rev. X **12**, 031028 (2022).

[63] N. P. de Leon, K. M. Itoh, D. Kim, K. K. Mehta, T. E. Northup, H. Paik, B. S. Palmer, N. Samarth, S. Sangtawesin, and D. W. Steuerman, Materials challenges and opportunities for quantum computing hardware, Science **372**, eabb2823 (2021).

[64] C. Shinei, Y. Masuyama, M. Miyakawa, H. Abe, S. Ishii, S. Saiki, S. Onoda, T. Taniguchi, T. Ohshima, and T. Teraji, Nitrogen related paramagnetic defects: Decoherence source of ensemble of NV^- center, J. Appl. Phys. **132**, 214402 (2022).

[65] U. Zvi, D. Candido, A. Weiss, A. Jones, L. Chen, I. Golovina, X. Yu, S. Wang, D. Talapin, M. E. Flatté, A. Esser-Kahn, and P. C. Maurer, Engineering spin coherence in core-shell diamond nanocrystals, arXiv:2305.03075.

[66] W. Yang and R.-B. Liu, Quantum many-body theory of qubit decoherence in a finite-size spin bath, Phys. Rev. B **78**, 085315 (2008).

[67] W. Yang and R.-B. Liu, Quantum many-body theory of qubit decoherence in a finite-size spin bath. II. Ensemble dynamics, Phys. Rev. B **79**, 115320 (2009).

[68] See Supplemental Material at http://link.aps.org/supplemental/10.1103/PhysRevMaterials.8.026204 for contains additional information about CCE calculations, materials processing, and NV center measurements.

[69] M. Annis, W. Cheston, and H. Primakoff, On statistical estimation in physics, Rev. Mod. Phys. **25**, 818 (1953).

[70] A. Cox, M. E. Newton, and J. M. Baker, ^{13}C, ^{14}N and ^{15}N endor measurements on the single substitutional nitrogen centre (PL) in diamond, J. Phys.: Condens. Matter **6**, 551 (1994).

[71] M. Onizhuk, K. C. Miao, J. P. Blanton, H. Ma, C. P. Anderson, A. Bourassa, D. D. Awschalom, and G. Galli, Probing the coherence of solid-state qubits at avoided crossings, PRX Quantum **2**, 010311 (2021).

[72] N. Zhao, S. W. Ho, and R. B. Liu, Decoherence and dynamical decoupling control of nitrogen vacancy center electron spins in nuclear spin baths, Phys. Rev. B **85**, 115303 (2012).

[73] X. Guo, N. Delegan, J. C. Karsch, Z. Li, T. Liu, R. Shreiner, A. Butcher, D. D. Awschalom, F. J. Heremans, and A. A. High, Tunable and transferable diamond membranes for integrated quantum technologies, Nano Lett. **21**, 10392 (2021).

[74] A. Tallaire, M. Kasu, K. Ueda, and T. Makimoto, Origin of growth defects in CVD diamond epitaxial films, Diam. Relat. Mater. **17**, 60 (2008).

[75] D. A. Broadway, N. Dontschuk, A. Tsai, S. E. Lillie, C. T.-K. Lew, J. C. McCallum, B. C. Johnson, M. W. Doherty, A. Stacey, L. C. L. Hollenberg, and J.-P. Tetienne, Spatial mapping of band bending in semiconductor devices using in situ quantum sensors, Nat. Electron. **1**, 502 (2018).

[76] J. N. Neethirajan, T. Hache, D. Paone, D. Pinto, A. Denisenko, R. Stöhr, P. Udvarhelyi, A. Pershin, A. Gali, J. Wrachtrup, K. Kern, and A. Singha, Controlled surface modification to revive shallow nv–centers, Nano Lett. **23**, 2563 (2023).